Inertial migration of spherical and oblate particles in a triangular microchannel

Junqi Xiong, Xuechao Liu, Huiyong Feng, and Haibo Huang*
Department of Modern Mechanics, University of Science and Technology of China, Hefei, Anhui 230026, People's Republic of China

(Received 16 August 2023; accepted 16 November 2023; published 11 December 2023)

The. inertial migration of both spherical and oblate particles within an equilateral triangular channel is studied numerically. Our study primarily focuses on the effects of fluid inertia, quantified by the Reynolds number (Re) and particle size (β). Our observations reveal two distinct equilibrium positions: the corner equilibrium position (CEP) is situated along the angle bisector near the corner, while the face equilibrium position (FEP) is located on a segment of the line perpendicular from the triangle's center to one of its sides. Spherical particles with varying initial positions predominantly reach the FEP. For oblate particles initially positioned along the angle bisector with a specific orientation, meaning the particle's evolution axis is inside the plane bisecting the angle, they will migrate along the angle bisector to reach the CEP while rotating in the tumbling mode. Conversely, for particles with different initial orientations and positions, they will employ the log-rolling mode to reach the FEP. Notably, we identify a dual-stage particle migration process to the FEP, with trajectories converging to an equilibrium manifold, which bears a resemblance to the cross section of the channel. To further illustrate the transition between FEP and CEP under general initial conditions, except for those along the angle bisector, we construct a phase diagram in the (Re, β) parameter space. This transition is often triggered by the size of larger particles (as the FEP cannot accommodate them) or the influence of inertia for smaller particles. For the FEP, especially for medium- or small-size particles, we notice an initial outward movement of the FEP from the center of the cross section as Re increases, followed by a return towards the center. This behavior results from the interplay of three forces acting on the particle. This research holds potential implications for the design of microfluidic devices, offering insights into the behavior of particles within equilateral triangular channels.

DOI: 10.1103/PhysRevE.108.065105

I. INTRODUCTION

Inertial migration, also referred to as inertial focusing, is an incredibly powerful technique for manipulating particle motion within microchannels [1,2]. Understanding the principles of inertial focusing is crucial in the design and optimization of efficient microfluidic devices used for particle separation, counting, detection, and sorting in suspensions [1,3]. The migration dynamics of particles in this phenomenon are influenced by a multitude of factors, including fluid properties, channel geometry, and particle characteristics.

The phenomenon of inertial migration of particles in a tube Poiseuille flow was initially reported by Segre and Silberberg [4]. In their experiment, particles accumulated at a specific radial position approximately 0.6 times the tube radius, forming what is known as the Segre-Silberberg annulus. Subsequent studies were conducted to explain the existence of the Segre-Silberberg annulus [5–8]. Ho and Leal [7] and Vasseur and Cox [8] used regular perturbation methods to identify a force called shear gradient lift force, which acts towards the walls of the channel. This force, along with the wall-induced center-directed force, establishes an equilibrium position in Poiseuille flow [1,9,10].

For plane or tube Poiseuille flow, analytical studies by Asmolov [11] and Matas *et al.* [12] revealed that the equilibrium position shifts towards the wall with increasing Reynolds number ($\mathrm{Re} = UL/\nu$), where U and L represent characteristic velocity and length, respectively, and ν denotes fluid dynamic viscosity. However, experimental results have shown the existence of additional equilibrium positions close to the channel center (inner annulus) in addition to the outer Segre-Silberberg annulus. The discrepancy between experimental and theoretical findings is attributed to the finite-size effect of particles [13]. More recently, Nakayama *et al.* [14] utilized experimental and numerical methods to further identify the presence of the inner annulus in tube Poiseuille flow.

In addition to circular tubes, curved and rectangular tubes have also been utilized to enhance particle focusing. Di Carlo *et al.* [15] were among the first to experimentally employ curved microchannels to concentrate randomly distributed particles into a single streamline. Rectangular ducts have also garnered attention in studies aiming to isolate particles in specific positions due to the presence of four face-centered equilibrium positions [16]. Under low to moderate Reynolds numbers (Re), particles in rectangular ducts migrate towards the four face centers [15–17]. However, when Re surpasses a critical value Re_c, new equilibrium positions near the corners emerge [18].

The control of particles in microchannels is significantly influenced by the cross-sectional shapes of the channels. In addition to circular and rectangular tubes, various other cross-sectional shapes have been investigated. Kim *et al.* [3] connected channels with circular, half-circular, and triangular cross sections to manipulate accessible focusing positions, successfully achieving particle focusing to a single stream

*huanghb@ustc.edu.cn; http://staff.ustc.edu.cn/~huanghb.

with 99% purity. Mukherjee *et al.* [19] focused particles into a single stream using low aspect ratio triangular microchannels with a tip angle of 120°. Subsequently, Kim *et al.* [20] experimentally studied the impact of particle size and Reynolds number (Re) on the number and location of inertial focusing positions in triangular microchannels with different tip angles.

For triangular cross sections with a tip angle of 60°, small particles were focused near the center of the wall, while stable focusing positions at the corners were observed for larger particles at Re = 20. As Re increased, the corner focusing positions disappeared. In the case of 120° channels, there were two focusing positions near the top corner and the center of the bottom wall, respectively. With increasing Re, the top and bottom focusing positions split and shifted towards the bottom angle along the side wall and bottom wall, respectively. These experiments demonstrated intriguing variations in inertial focusing positions, highlighting potential applications in various microdevices [3,19,20].

However, it is important to note that there are certain limitations in these experiments, particularly in terms of measuring the comprehensive migration dynamics of individual particles, including their trajectory, velocity, and rotation. Obtaining such measurements is challenging, yet it is essential for revealing the underlying fluid mechanism. Additionally, the reasons behind the variations in the equilibrium position of particles in triangular channels with respect to particle size and Reynolds number (Re) remain an open question.

Furthermore, in many practical applications, nonspherical particles are commonly encountered [2], such as cell separation. Red blood cells (RBCs) are a major component of human blood cells and their innate shape is closer to oblate spheroids. Motivated by this, our study is dedicated to investigating the migration of oblate particles within triangular channels. Given the biological relevance of oblate shapes and the lack of prior comprehensive studies on their migration dynamics, we expect our focus on oblate particles to provide insights that can help advance techniques for the separation and control of biologically important cells such as RBCs.

In this study, we numerically investigate the inertial migration of single sphere or oblate particles in triangular channels. The primary focus of this work is to examine the influence of Reynolds number, particle size, and shape on the migration dynamics and distribution of equilibrium positions. The paper is organized as follows: Section II introduces the simulation method and describes the physical problem. Section III presents the results and discussions regarding the migration of sphere and ellipsoid particles. Finally, the conclusions are summarized in Sec. IV.

II. NUMERICAL METHOD AND PROBLEM

A. Lattice Boltzmann method

The lattice Boltzmann method (LBM) is used to solve the incompressible Navier-Stokes equations and the immersed moving boundary (IMB) method [21] is used to deal with the fluid-particle coupling.

The popular Bhatnagar Gross Krook (BGK) model with single relaxation time τ is used and the evolution equation with an external force term is

$$f_\alpha(\boldsymbol{x}+\boldsymbol{e}_\alpha\delta t, t+\delta t) - f_\alpha(\boldsymbol{x}, t) = \Omega_\alpha^{\mathrm{BGK}} + \delta t f_\alpha,$$

where $f_\alpha(\boldsymbol{x}, t)$ is the particle distribution function, and $\Omega_\alpha^{\mathrm{BGK}}$ and $f_\alpha^{\mathrm{eq}}(\boldsymbol{x}, t)$ are the collision term and equilibrium particle distribution function, respectively. They are written as

$$\Omega_\alpha^{\mathrm{BGK}} = -\frac{\delta t}{\tau}\left[f_\alpha(\boldsymbol{x}, t) - f_\alpha^{\mathrm{eq}}(\boldsymbol{x}, t)\right] \tag{1}$$

and

$$f_\alpha^{\mathrm{eq}}(\boldsymbol{x}, t) = \rho\omega_\alpha\left[1 + \frac{\boldsymbol{e}_\alpha\cdot\boldsymbol{u}}{c_s^2} + \frac{(\boldsymbol{e}_\alpha\cdot\boldsymbol{u})^2}{2c_s^4} - \frac{\boldsymbol{u}^2}{2c_s^2}\right]. \tag{2}$$

The last term f_α represents the effect of external force and is calculated as [22]

$$f_\alpha = \left(1 - \frac{1}{2\tau}\right)\omega_\alpha\left[\frac{\boldsymbol{e}_\alpha - \boldsymbol{u}}{c_s^2} + \frac{(\boldsymbol{e}_\alpha\cdot\boldsymbol{u})}{c_s^4}\boldsymbol{e}_\alpha\right]\cdot\boldsymbol{F}, \tag{3}$$

where $\boldsymbol{F}$ is the macroscopic external force term. The macroscopic density ρ and macroscopic velocity $\boldsymbol{u}$ can be obtained through

$$\rho = \sum_{\alpha=0}^{8} f_\alpha, \quad \rho\boldsymbol{u} = \sum_{\alpha=0}^{8}\boldsymbol{e}_\alpha f_\alpha + \frac{\boldsymbol{F}\delta t}{2\rho}. \tag{4}$$

In our three-dimensional LBM simulations, the D3Q19 velocity model is adopted. The 19 discrete velocities $\boldsymbol{e}_\alpha$ are defined as

$$\boldsymbol{e}_\alpha = \begin{cases} (0,0,0)c, & \alpha = 0 \\ (\pm1,0,0)c,\ (0,\pm1,0)c,\ (0,0,\pm1)c, & \alpha = 1-6 \\ (\pm1,\pm1,0)c,\ (\pm1,0,\pm1)c,\ (0,\pm1,\pm1)c, & \alpha = 7-18. \end{cases} \tag{5}$$

The corresponding weighting parameters ω_α are $\omega_0 = 1/3$, $\omega_{1-6} = 1/18$, $\omega_{7-18} = 1/36$.

The lattice speed c is given by $c = \frac{\delta x}{\delta t}$, where δx is the lattice size and δt is the time step. $c_s^2 = c^2/3$ is the lattice sound speed. In our simulations, we use the lattice units, i.e., $\delta x = 1$ lattice unit (lu) and $\delta t = 1$ time step (ts).

B. Solid particle dynamics and fluid-solid boundary interaction

The translational motion of the particle is controlled by Newton's second law, which is described as

$$m\frac{d^2\boldsymbol{x}_c}{dt^2} = \boldsymbol{F}_h, \tag{6}$$

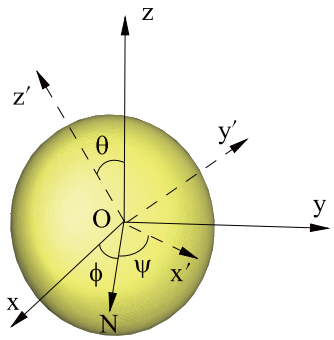

FIG. 1. Sketch of an oblate particle with the symmetric axis (x' axis). $Oxyz$ and $Ox'y'z'$ denote the space-fixed and body-fixed frames, respectively. (ϕ, θ, ψ) represents the Euler angles.

where m is the mass of the suspended particle. The rotation of the particle is determined by the Euler equation and is written as

$$\boldsymbol{I}\frac{d\boldsymbol{\omega}_p}{dt} + \boldsymbol{\omega}_p \times [\boldsymbol{I}\cdot\boldsymbol{\omega}_p] = \boldsymbol{T}_h, \tag{7}$$

where $\boldsymbol{I}$ is the inertial tensor and $\boldsymbol{\omega_p}$ is the angular velocity of the particle.

The above equation governing the particle rotation is solved in a body-fixed coordinate system and the coordinate transformation matrix is needed. As shown in Fig. 1, in a body-fixed coordinate system, the oblate ellipsoid is described by

$$\frac{x'^2}{a^2} + \frac{y'^2}{b^2} + \frac{z'^2}{c^2} = 1. \tag{8}$$

In the body-fixed coordinate system, the inertial tensor is diagonal and the principal moments of inertia are

$$I_{x'x'} = m\frac{b^2+c^2}{5}, \quad I_{y'y'} = m\frac{a^2+c^2}{5}, \quad I_{z'z'} = m\frac{a^2+b^2}{5}. \tag{9}$$

In this study, Euler angles (ϕ, θ, ψ) are used to describe the rotation of the particle. Suppose that initially, the body-fixed coordinate system coincides with the space-fixed coordinate system $Oxyz$, and the symmetry axis of the spheroid aligns with the x' direction. The particle undergoes a series of rotations: first around the z' axis by an angle ϕ, then around the new x' axis by an angle θ, and finally around the z' axis again by an angle ψ.

In our simulation, we employ the immersed moving boundary (IMB) method to handle fluid-structure coupling. The IMB method was initially proposed by Noble and Torczynaski [21] and has been used for simulating particle flow with the discrete element method (DEM) by Cook *et al.* [23]. This method has been widely employed in various engineering problems involving particles, such as erosion [23], dredging [24], and electromagnetic excitation of particle suspensions [25].

In the IMB approach, an additional collision term Ω_i^s is incorporated into the standard evolution equation of the LBM, accounting for the interactions with solid obstacles within the computational cell [23]. To enforce the no-slip condition, the modified evolution equation is expressed as follows [21,23]:

$$f_\alpha(\boldsymbol{x}+\boldsymbol{e}_\alpha\delta t, t+\delta t) = f_\alpha(\boldsymbol{x},t) + [1-B_s]\Omega_\alpha^{\mathrm{BGK}} + B_s\Omega_\alpha^S + \delta t F_\alpha, \tag{10}$$

where B_s is a weighting function. B_s is calculated as

$$B_s = \frac{\epsilon(\tau/\delta t - 1/2)}{(1-\epsilon)+(\tau/\delta t - 1/2)}, \tag{11}$$

where ϵ is the local solid fraction on the lattice cell.

Ω_α^s, which is based on the concept of bounce-back of the nonequilibrium part of the particle distribution, is used [21],

$$\Omega_\alpha^s = f_{-\alpha}(\boldsymbol{x},t) - f_\alpha(\boldsymbol{x},t) + f_\alpha^{\mathrm{eq}}(\rho,\boldsymbol{U}_s) - f_{-\alpha}^{\mathrm{eq}}(\rho,\boldsymbol{u}), \tag{12}$$

where $f_{-\alpha}$ denotes the particle distribution function along the reverse α direction, and $\boldsymbol{U}_s$ is the particle's velocity.

The total hydrodynamic force and torque acting on the particle are calculated by

$$\boldsymbol{F}_h = \frac{\delta x^2}{\delta t}\sum_n B_s^n \sum_\alpha \Omega_\alpha^s \boldsymbol{e}_\alpha, \tag{13a}$$

$$\boldsymbol{T}_h = \frac{\delta x^2}{\delta t}\sum_n (\boldsymbol{x}_n - \boldsymbol{x}_c)\times B_s^n \sum_\alpha \Omega_\alpha^s \boldsymbol{e}_\alpha, \tag{13b}$$

where $\boldsymbol{x}_c$ is the center of mass of the solid particle.

TABLE I. The dimensionless equilibrium position r^* and the particle velocities u^* and ω^* at the equilibrium position. r, u, and ω are normalized by R, u_m, and u_m/R, respectively.

	r^*	u^*	ω^*
LBM (Present)	0.597	0.619	0.580
ALE (Yang *et al.*)	0.601	0.620	0.581
DLM (Yang *et al.*)	0.606	0.610	0.579

C. Validation of the numerical method

Our simulation code was validated using a sphere moving in a tube Poiseuille flow, as depicted in Fig. 2(a). In these simulations, the sphere and tube have radii a and R, respectively, with a ratio of $a/R = 0.15$. The Reynolds number is calculated as $\mathrm{Re}_t = \frac{8a^2u_m}{\nu R} = 9$, where u_m represents the maximum flow velocity. Two types of simulations were conducted: unconstrained and constrained. In the unconstrained simulation, the particle is free to move and migrates towards an equilibrium position. Table I presents the dimensionless final equilibrium position and particle velocities. Our simulation results align well with those obtained using the arbitrary Lagrangian-Eulerian (ALE) moving mesh and the distribution of Lagrange multipliers (DLM) methods [26]. In the constrained simulations, the lateral migration of the particle is suppressed and the radial position remains fixed. The particle is allowed to move solely along a line parallel to the tube's axis, while being able to rotate freely. Figure 2 illustrates the particle velocities and the hydrodynamic lift force experienced by the particle as functions of the radial position once

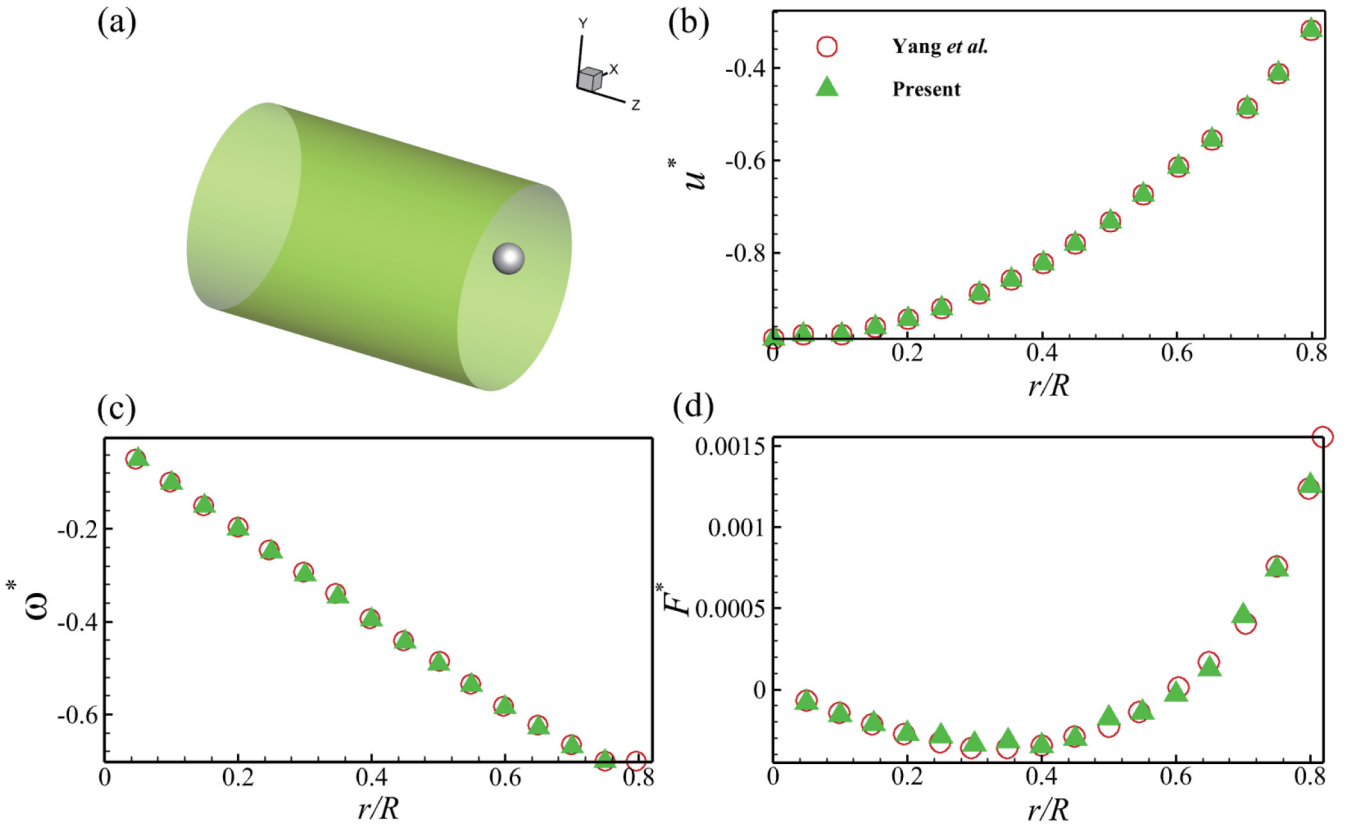

FIG. 2. (a) Sketch of a sphere in a tube Poiseuille flow. Dimensionless steady-state values of velocities (b) u^*, (c) ω^*, and (d) the lift force F^* with different radial positions. F is normalized by $\rho u_m^2 R^2$.

the particle reaches a steady state. Our results exhibit good agreement with the findings presented in [26].

D. Flow problem

In this study, we investigate the inertial migration of neutrally buoyant particles in triangular microchannels. The focus is on particles moving within a microchannel that has an equilateral triangular cross section, as illustrated in Fig. 3. The

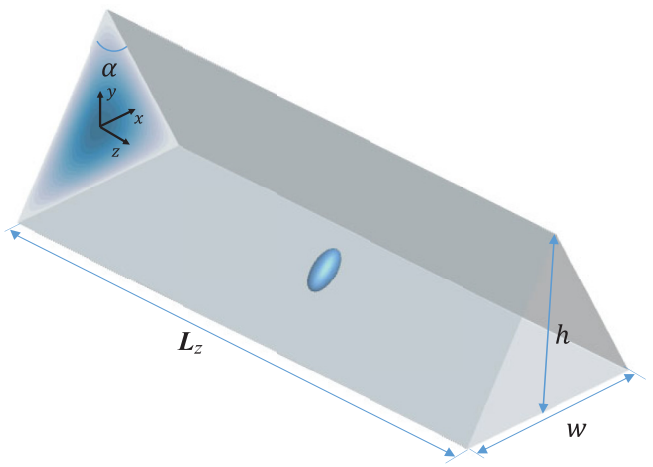

FIG. 3. Sketch of a particle in a triangular channel Poiseuille flow. Here, h and w are the height and width of the equilateral triangular cross section, respectively. L_z is the channel length.

equilateral triangle is characterized by its height h and width w. The length of the channel is L_z.

In our analysis of nonspherical particles, we specifically focus on oblate particles. An oblate particle is characterized by having the inequality $a < b = c$, where a represents the major semi-axis and $b = c$ denotes the minor semi-axes. The aspect ratio (Ar) is defined as the ratio of the minor semi-axis (b) to the major semi-axis (a). Additionally, we define the effective radii of oblate particles as $r_e = (abc)^{1/3}$. This implies that the oblate particle has the same volume as a sphere with a radius of r_e. The corresponding effective diameter is given by $d_e = 2r_e$.

In our investigation, we introduce the blockage ratio (β) to quantify the degree of obstruction caused by the presence of a particle within the channel,

$$\beta = \frac{d_e}{D_t}, \tag{14}$$

where D_t is the hydraulic diameter of the equilateral triangle. In this study, the size of the channel remains constant, and the parameter β represents the size of the particle. The range of β is set to be between 0.115 and 0.46. Figure 4 illustrates the cross-sectional sketches of small, medium, and large particles within the channel.

The Reynolds number Re is defined as

$$\mathrm{Re} = \frac{U_a D_t}{\nu}, \tag{15}$$

where U_a is the average velocity.

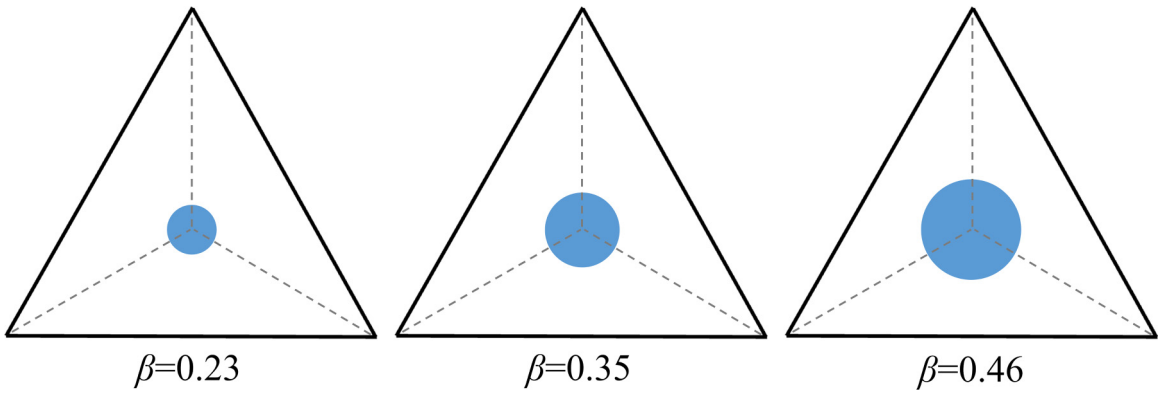

FIG. 4. The sketches of small, medium, and large spherical particles (from left to right, $\beta = [0.23, 0.35, 0.46]$, respectively).

In the subsequent analysis, we investigate the influence of β and Re on the migration dynamics of both spherical and oblate particles in the triangular microchannels. The channel walls are subject to no-slip boundary conditions implemented using the interpolated bounce-back method [27]. To induce Poiseuille flow, a constant body force in the z-axis direction is applied, while periodic boundary conditions are employed in the flow direction. To ensure the reliability of our results, we conduct a grid independence study and examine the effect of the channel length in the flow direction, as illustrated in Fig. 5. Our findings indicate that using $w = 150\ lu$ and $L_z = 20d_e$ yields grid- and channel-length-independent results. Hence, these parameter values are utilized in the subsequent investigations.

III. RESULTS AND DISCUSSION

A. Migration of a spherical particle

In this section, we will examine the migration of a sphere in the triangular channel. The particles will undergo migration and settle into equilibrium positions due to the fluid-particle interaction. Two equilibrium positions, i.e., corner equilibrium position and face equilibrium position, will be discussed in detail. The effects of the initial position, Re, and particle size (β) will be investigated.

1. Effect of initial position

First, we investigate the effect of different initial positions of the particle on the final equilibrium within the channel. Figure 6 illustrates several representative trajectories of particle migration, considering five typical initial positions. In these cases, $\mathrm{Re} = 20$ and $\beta = 0.23$.

Our observations reveal the presence of two types of equilibrium positions within the channel. The corner equilibrium position (CEP) is situated along the angle bisector near the corner, which is denoted by the green hollow triangle, while the face equilibrium position (FEP) is located close to the middle of each face, along the mediator of that face, which is represented by the red hollow triangle. Due to symmetry, in total, there are six equilibrium positions within the channel. The result aligns with conclusions obtained in previous studies [20].

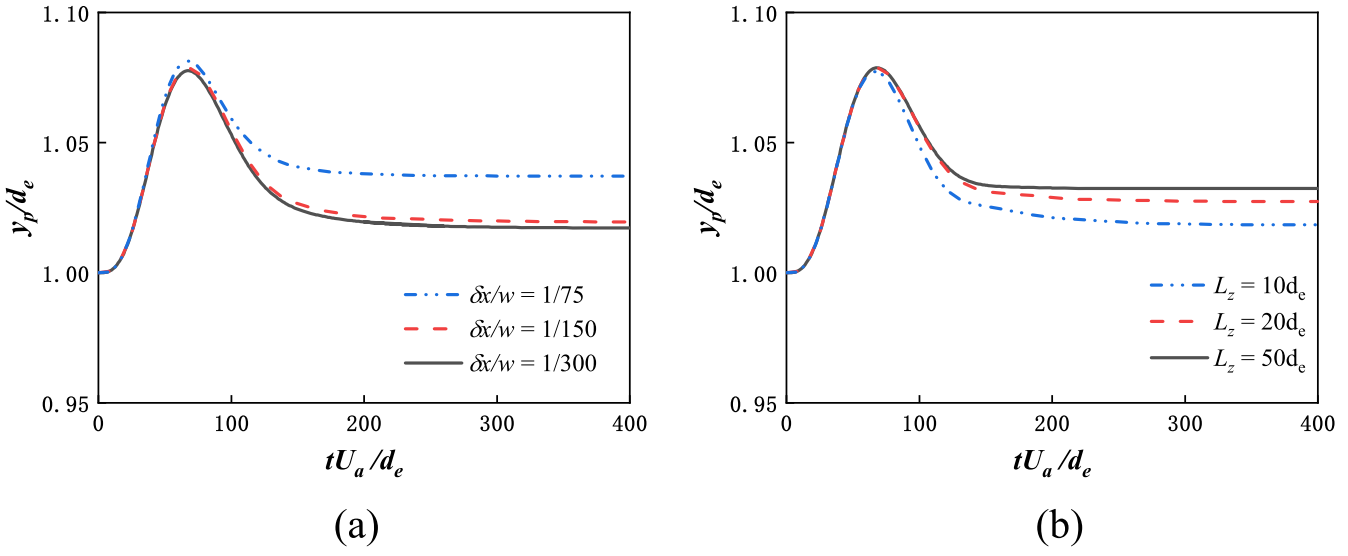

FIG. 5. Effects of (a) grid size and (b) channel length on the migration of an oblate particle ($\mathrm{Ar} = 0.5$, $\beta = 0.23$ and $\mathrm{Re} = 200$). For simulations in (a), $L_z = 20d_e$ is used, and in (b), $\delta x/w = 1/150$ is used.

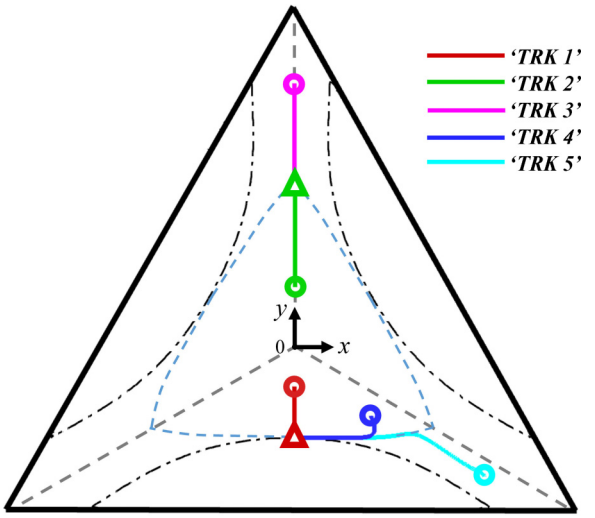

FIG. 6. Inertial migration of particles in an equilateral triangle channel (Re = 20, $\beta = 0.23$). Solid lines with different colors represent particle trajectories. The hollow circles indicate the initial positions of the particles, and the hollow triangles represent the equilibrium positions. The black dash-dotted lines denote the contours of the shear rate at the equilibrium position. Contours traversing the CEP are not depicted for the sake of clarity. The blue dashed line corresponds to the particle equilibrium manifold.

For particles initially exactly located on the angle bisector ('TRK1', 'TRK2', 'TRK3' in Fig. 6), they migrate towards equilibrium positions along the angle bisector, under the influence of vertical forces. However, particles initially situated in other positions ('TRK4', 'TRK5') exhibit nonlinear migration trajectories. These nonlinear trajectories can be divided into two stages: the first stage involves migration towards the wall, followed by the second stage where the trajectories become parallel to the wall. Remarkably, in the second stage, the trajectories of particles originating from different initial positions collapse onto the equilibrium manifold, depicted by the blue dashed line. This equilibrium manifold bears a resemblance to the cross section of the channel and tangentially intersects a certain shear rate contour represented by the black dashed line. It is noted that the particle migration behavior in rectangular channels exhibits similarities to the two stages mentioned above [28].

We would like to discuss the mechanism in the two stages. Figure 7 provides an overview of the migration of the sphere for 'TRK2', as shown in Fig. 6. In the first stage, the particle's motion is primarily influenced by the shear-induced lift force ($\boldsymbol{F}_{\mathrm{S}}$) and the wall-induced lift force ($\boldsymbol{F}_{\mathrm{W}}$). Notably, due to the unequal distances between the particle and the three walls, the wall forces acting on the particle do not align perfectly in the vertical direction. Under the influence of $\boldsymbol{F}_{\mathrm{S}}$ and $\boldsymbol{F}_{\mathrm{W}}$, the particle moves toward the wall and eventually becomes attracted to the equilibrium manifold [28], where $\boldsymbol{F}_{\mathrm{S}}$ and $\boldsymbol{F}_{\mathrm{W}}$ are balanced. The first stage is rapid and it takes approximately 10 times less than the second stage in our simulations.

In the second stage, owing to the large shear experienced by the particle while being close to the wall, the contribution of the rotation-induced lift force ($\boldsymbol{F}_{\Omega}$) becomes significant. A previous study by Cherukat and McLaughlin [29] confirms this observation. The direction of $\boldsymbol{F}_{\Omega}$ is determined by the cross product of the rotation vector and the relative particle velocity vector, represented as $\boldsymbol{F}_{\Omega} = \boldsymbol{\Omega} \times \boldsymbol{U}_{\mathrm{r}}$. The directions of $\boldsymbol{\Omega}$ and $\boldsymbol{U}_{\mathrm{r}}$ are labeled in the figure. According to this formula, $\boldsymbol{F}_{\Omega}$ points towards the negative x axis, causing the particle to migrate parallel to the wall and reach its equilibrium position.

To demonstrate that the second stage is primarily a result of $\boldsymbol{F}_{\Omega}$, we have conducted further investigations. Figure 8(a) illustrates two distinct cases, denoted as case I and case II. In both cases, we initiated particle positions at point A on the manifold. In case I, the particle was allowed to move and rotate freely, while in case II (the nonrotating case), the particle could only translate but was constrained from rotating.

Our findings unequivocally reveal that the free particles migrated to point B, which corresponds to the FEP, whereas the nonrotating particles moved to point C. This stark contrast signifies that nonrotating particles were unable to migrate along the manifold towards the FEP, while the free particles, influenced by $\boldsymbol{F}_{\Omega}$, exhibited lateral motion during the second stage.

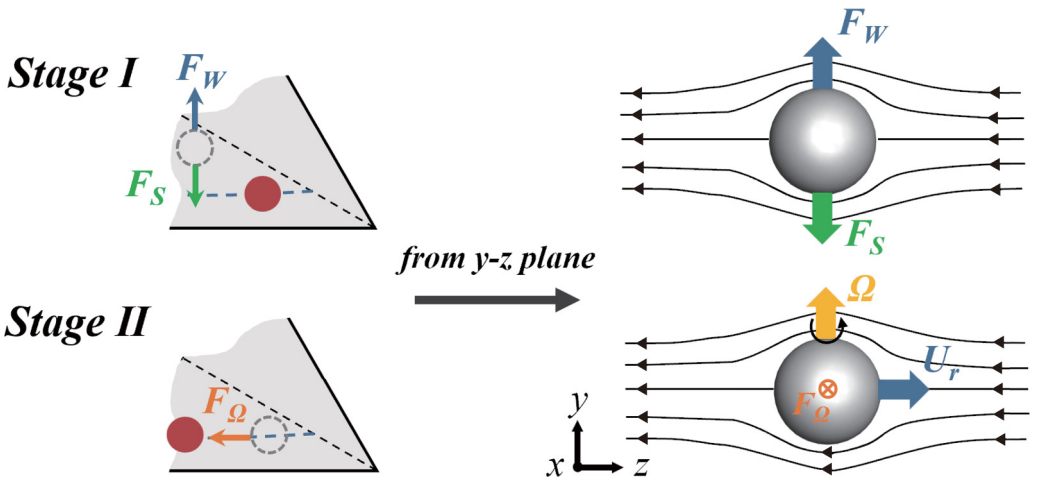

FIG. 7. The particle experiences the shear-induced lift force $\boldsymbol{F}_{\mathrm{S}}$ and the wall-induced force $\boldsymbol{F}_{W}$ during the first stage, and the rotation-induced lift force $\boldsymbol{F}_{\Omega}$ becomes significant in the second stage.

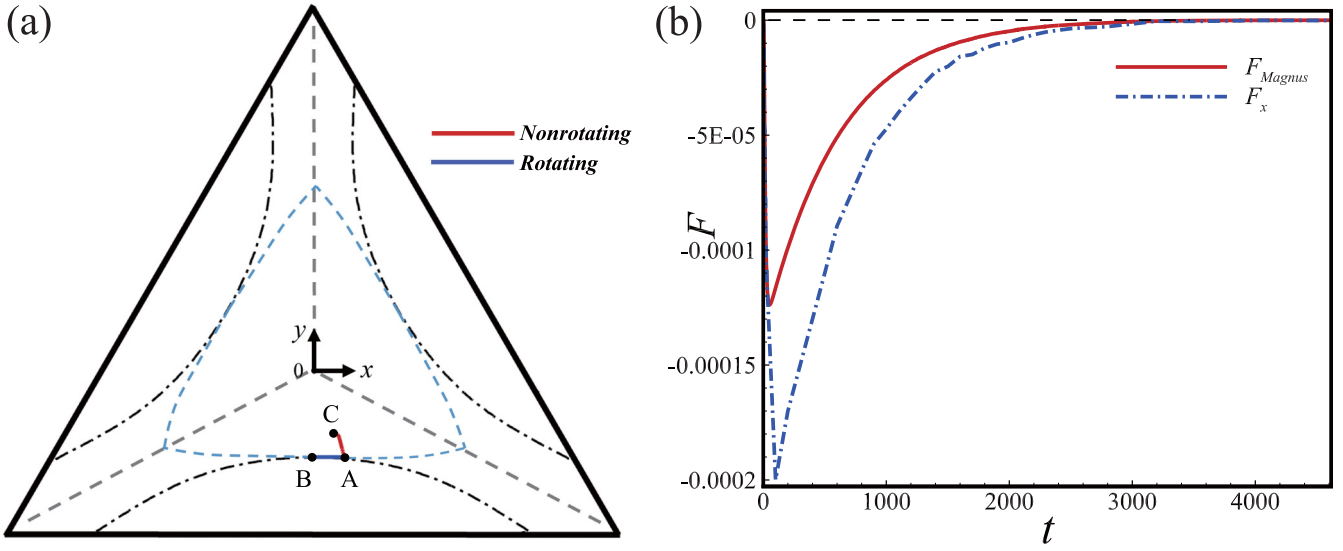

FIG. 8. (a) The migration trajectories of nonrotating and rotating cases. Point A is the initial position. The blue and red solid lines represent the trajectories of rotating and nonrotating particles, respectively. Points B and C represent their final equilibrium positions. Re $= 20$, $\beta = 0.23$. (b) Forces on the rotating particle during its migration toward the FEP. The red curve represents the Magnus force and the blue dashed line represents the lift force.

There is one more thing that needs to be clarified, which is why the leftward lift force is mainly "rotation induced" during the second stage. We conduct a comparison of the magnitudes of the lift force and the Magnus force. This comparison is presented in Fig. 8(b), in which both the lift force and the Magnus force acting on the particle during its migration toward the FEP are illustrated. The Magnus force (red curve) is calculated theoretically based on the angular velocity $\boldsymbol{\omega}$ obtained from our LBM simulation and the Magnus formula $\boldsymbol{F}_L = S\boldsymbol{\omega} \times \boldsymbol{v}$, where S is the average coefficient of fluid resistance and $\boldsymbol{v}$ is the relative velocity vector. The blue dashed curve depicts the lift force directly obtained from our LBM simulation. We note a consistent alignment in the trends of these two forces. That means the lift force is mainly contributed by the Magnus force, i.e., the lift force is truly rotation induced. The minor discrepancy between the two curves is attributed to the two other forces (F_S and F_W). Therefore, we confirm that the lift force is mainly rotation induced.

In the following sections, we will concentrate on quantitatively examining the effects of β and Re on the CEP and FEP.

2. The corner equilibrium position

In this section, we first examine the impact of β and Re on the equilibrium position. Subsequently, to gain a deeper understanding of particle behavior, we analyze the forces acting on particles. During this analysis, particles are allowed to move along a line parallel to the flow direction and rotate freely, while lateral migration is suppressed.

In this section, we will investigate the variation of the CEP in response to changes in Re and β. It should be noted that at a specific Re, the CEP remains independent of the initial locations along the angle bisector. The subsequent analyses are based on trajectories similar to 'TRK2' in Fig. 6.

Figure 9(a) presents the variation of y_p^* (normalized y coordinate of the equilibrium position) with β for different Re values. The movement of the equilibrium position with changes in Re and β displays an opposite trend: the equilibrium position moves further away from the center of the channel as Re increases at a specific β, and it gets closer to the center as β increases at a specific Re.

To gain a better understanding of this particle behavior, we examined the lift coefficient of the particles during their motion. The lateral forces exerted on the particle were calculated. In these simulations, the particles were allowed to move along a line parallel to the flow direction and rotate freely, while the lateral migration was suppressed. The situation is similar to the cases in the above numerical validation part (Sec. II C).

The lift coefficient $\boldsymbol{C}_\mathrm{L} = (C_\mathrm{Lx}, C_\mathrm{Ly})$ is defined as

$$\boldsymbol{C}_\mathrm{L} = \frac{\boldsymbol{F}_\mathrm{L}}{\rho \dot{\gamma}^2 a^4}, \tag{16}$$

where $\boldsymbol{F}_\mathrm{L}$ is the lateral force on the particle in the opposite direction of its crossflow velocity, ρ is the fluid density, and a is the particle radius.

As shown in Fig. 10 (cases of $\beta = 0.23$), we have examined the maps of the lateral force coefficient $\boldsymbol{F}_\mathrm{L}$ on the channel cross section. Each arrow represents a case in which particles can solely move along the z direction and rotate. In our simulated cases, the initial position of the particles is below the CEP. First, we observe that the CEP is a saddle point; even a minor disturbance applied to the particle will cause it to move away from this equilibrium position. It is indicated by an empty triangle symbol near the apex of the triangle in Fig. 10.

Second, through this figure, we can elucidate the movement of equilibrium positions. Now, it is important for us to consider the three forces acting on the particle, namely, $\boldsymbol{F}_\mathrm{S}$, $\boldsymbol{F}_\mathrm{W}$, and $\boldsymbol{F}_\Omega$. Figure 11(a) illustrates the orientations of the rotations and forces experienced by particles migrating to the CEP and FEP, respectively. It is evident that the directions of $\boldsymbol{F}_\mathrm{S}$ and $\boldsymbol{F}_\Omega$ are consistently aligned and opposite to that of

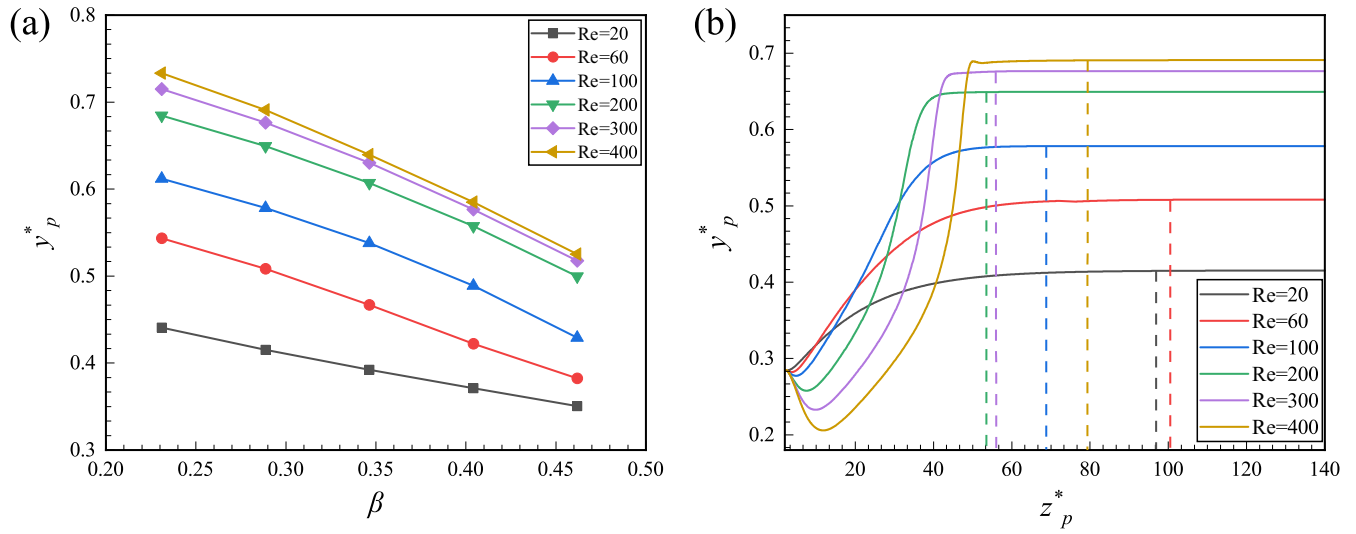

FIG. 9. The effect of Re and β on the CEP: (a) Dimensionless vertical equilibrium position y_p^* as a function of blockage ratio β under different Re. The initial position of each point is $(x_p^*, y^*p) = (0, 0.28)$. (b) Dimensionless vertical position y_p as a function of focusing length (dimensionless stream length z_p^*) under different Re with $\beta = 0.29$.

$\boldsymbol{F}_W$. Therefore, we can evaluate the magnitudes of $\boldsymbol{F}_S + \boldsymbol{F}_\Omega$ and $\boldsymbol{F}_W$.

In the region below the CEP in Fig. 10, the net force is upward and is dominated by $\boldsymbol{F}_S + \boldsymbol{F}_\Omega$. The local shear-induced lift force $\boldsymbol{F}_S$ is significantly influenced by Re. As Re increases, the region where $|\boldsymbol{F}_S + \boldsymbol{F}_\Omega| > |\boldsymbol{F}_W|$ moves up, leading to the equilibrium position being pushed further away from the center.

Conversely, as β increases, the particle's border becomes closer to the walls. Here, $\boldsymbol{F}_W$, which pushes the particle away from the wall, grows significantly. The region where $|\boldsymbol{F}_W| > |\boldsymbol{F}_S + \boldsymbol{F}_\Omega|$ moves down. As a result, the CEP becomes closer to the center.

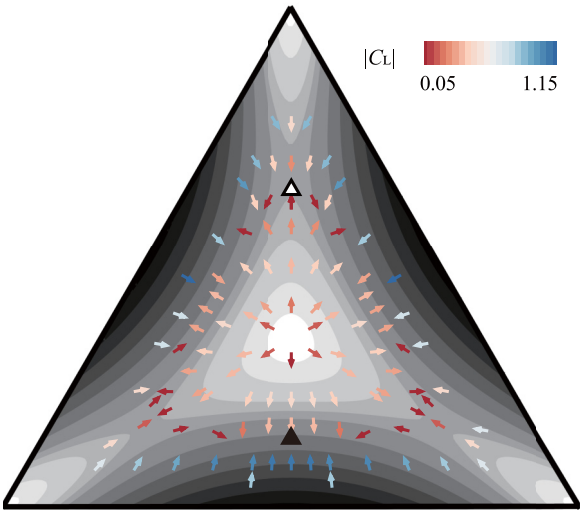

FIG. 10. Net lift force coefficient $\boldsymbol{C}_L$ over triangular channels. The arrows represent the direction, and the colors denote the magnitude of $\boldsymbol{C}_L$. The background represents the shear rate contour. The hollow triangle represents the saddle point, and the solid represents the stable equilibrium position. Re = 20 and $\beta = 0.23$ are fixed.

To demonstrate the validity of the above conclusion, we conduct two representative simulations, as shown in Fig. 11(b). The first simulation aimed to investigate the impact of particle size (β) on the CEP. In this simulation, we initially placed a larger particle at position A, which is the terminal equilibrium location for a smaller particle, and then released it to observe its trajectory. It was observed that the larger particles moved towards point B, away from the wall. This indicates the dominance of $\boldsymbol{F}_W$, i.e., $|\boldsymbol{F}_W| > |\boldsymbol{F}_S + \boldsymbol{F}_\Omega|$. The second simulation involved increasing the Reynolds number (Re) while particles initially moved from equilibrium position A at Re = 20. As we increased the Reynolds number to Re = 100, the particle gradually moved away from the center towards point C, suggesting the dominance of $\boldsymbol{F}_S + \boldsymbol{F}_\Omega$, i.e., $|\boldsymbol{F}_S + \boldsymbol{F}_\Omega| > |\boldsymbol{F}_W|$. A similar analysis is also applicable to the FEP. We believe that this explanation will facilitate better reader comprehension.

In summary, for the CEP, a larger particle tends to be closer to the center of the cross section, while increasing Re pushes it away from the center.

In a previous study [28], an optimal value of Re was identified, which corresponds to the minimum focusing length (the length of particle migration along the flow direction, i.e., z direction). Figure 9(b) illustrates the variation of the focusing length for particles with $\beta = 0.29$ at different Re. Among these, when Re = 200, it is considered the optimal Re that provides the minimum focusing length.

3. The face equilibrium position

Most particles from diverse initial positions (excluding the angle bisector) tend to migrate towards the FEP (see Fig. 6). Depending on Re or β, the particles may also migrate to the CEP, which will be discussed in the next section. In this section, our primary focus is on the FEP, which serves as a stable equilibrium position, unlike the CEP.

Figure 12(a) presents the variation of y_p^* with Re for different β. As β increases with fixed Re, the equilibrium position

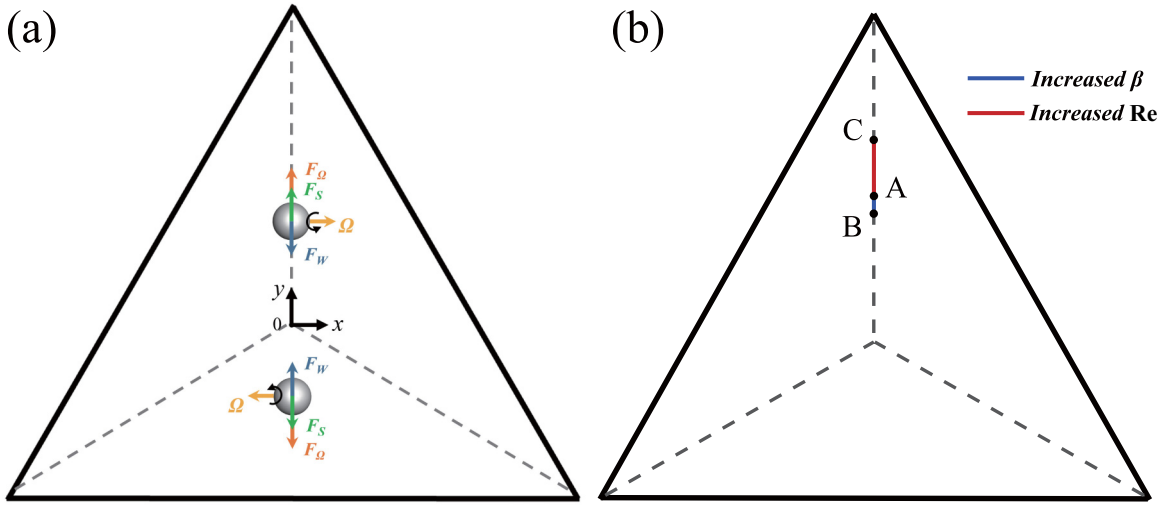

FIG. 11. (a) Directions of the rotations and forces acting on particles in the triangular channel. These two particles migrate to the CEP and FEP, respectively. (b) Trajectories of particles with increased β and Re. Point A represents the equilibrium position of the particle at $\beta = 0.23$ and $\mathrm{Re} = 20$. Point B represents the equilibrium position when β is increased to $\beta = 0.35$. Point C represents the equilibrium position when Re is increased to $\mathrm{Re} = 100$.

moves closer to the center of the channel. This observation aligns with the explanation from the previous section, where the wall-induced lift force increases faster and pushes it closer to the center as β increases.

However, with a fixed β, the equilibrium position is initially far away from the center and then moves closer as Re increases. For all β values, the closest distance to the wall is observed at $\mathrm{Re} = 100$. To understand this phenomenon, we should pay attention to the position of FEP in Fig. 10 at this specific Re. Near the FEP, the closer the particle is to the wall, the larger the lift coefficient pointing toward the center (indicated by the red arrow at the bottom).

At the beginning of increasing Re, $\boldsymbol{F}_S + \boldsymbol{F}_\Omega$ dominate, leading to the equilibrium position being away from the center. However, as Re increases further, the particles can no longer get close to the wall due to the high lift coefficient pointing towards the center. This results in an upward movement of the equilibrium position.

Next, we would like to discuss the focusing length. Figure 12(b) illustrates the variation of the focusing length for particles with $\beta = 0.35$ at different Re. It is seen that there is an optimal $\mathrm{Re} \approx 60$, which has the shortest focusing length. It appears that there is no correlation between the optimal Re case and the case with the closest distance to the wall.

4. The transition between the FEP and CEP

When the particle's initial position lies on the bisector of the angle, the equilibrium position (CEP) remains unchanged. However, for particles located at other positions in the chan-

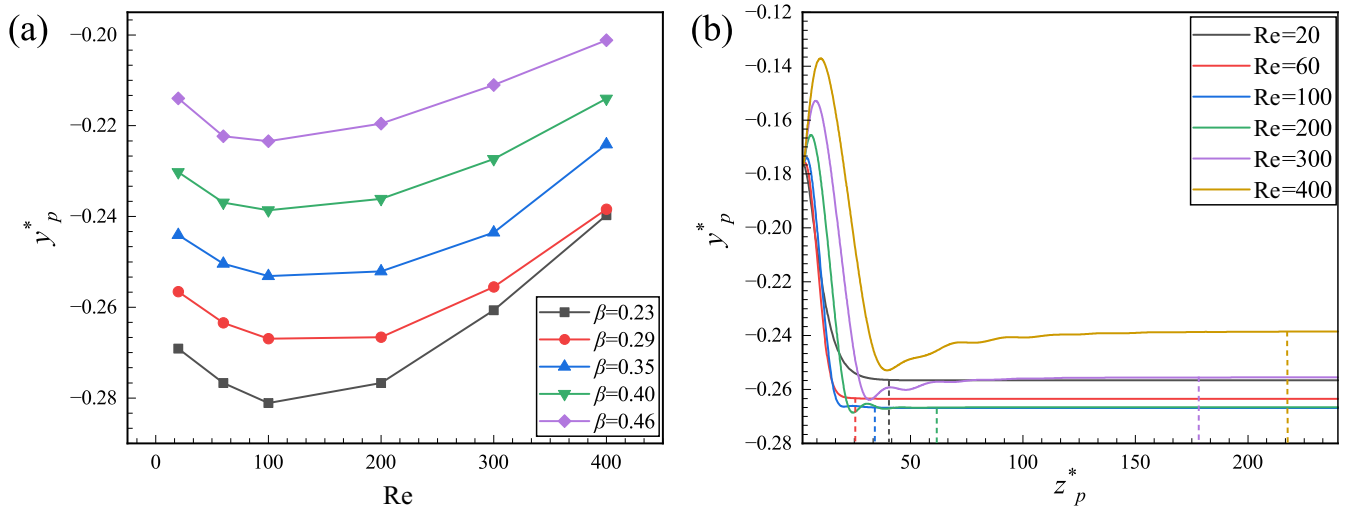

FIG. 12. The effect of Re and β on the face equilibrium position: (a) Dimensionless vertical equilibrium position y_p^* as a function of blockage ratio Re under different β. The initial position of each point is $(x_p^*, y_p^*) = (0, -0.18)$. (b) Dimensionless vertical position y_p^* as a function of focusing length under different Re with $\beta = 0.35$.

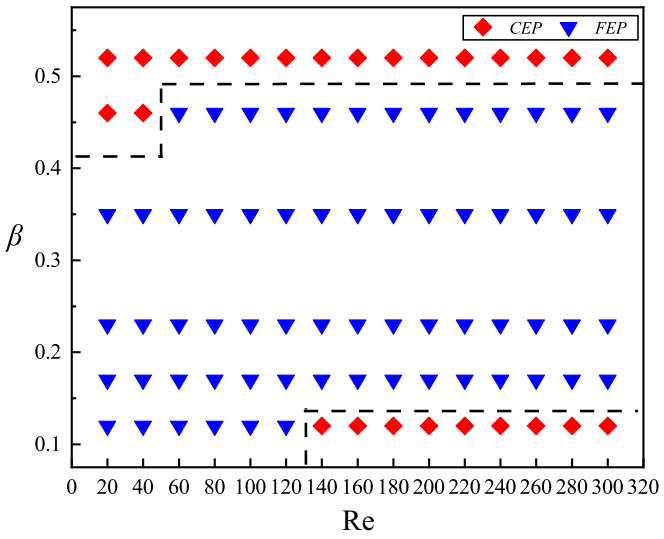

FIG. 13. Phase diagram of particle equilibrium positions in the (Re, β) parameter plane. The red diamond represents the corner equilibrium position (CEP), and the blue inverted triangle represents the center-edge equilibrium position (FEP). The initial position of each point is $(x_p^*, y_p^*) = (0.23, -0.2)$.

nel, the final equilibrium position is influenced by both Re and β. In this section, we take cases such as 'TRK2' (that share the same initial position) as an example to explore the migration of particles in general positions within the channel.

Figure 13 illustrates the variation of the particle's equilibrium position with respect to Re and β. For large particles ($\beta = 0.46$), the equilibrium position transitions from the CEP to the FEP. This is because as Re increases, the FEP first approaches and then moves away from the wall, allowing it to accommodate larger particles. For larger particles ($\beta > 0.46$), they can only stay at the CEP since the FEP can no longer accommodate excessively large particles.

For medium particles ($0.15 < \beta < 0.4$), the equilibrium position remains at the FEP. This is because these particles initially tend towards the FEP and maintain this state due to inertia.

For small particles ($\beta = 0.12$), the equilibrium transitions from FEP to CEP around Re ≈ 120. As fluid inertia escalates with increasing Re, the particle's inertia remains constant. As a result, particles primarily align with the flow direction. If a small particle resides in the FEP at higher Re, the rapid flow velocity and significant shear gradient (refer to Fig. 9) might disrupt the equilibrium. Consequently, these particles are carried towards the CEP, characterized by lower flow velocity and milder shear gradient, ensuring a more stable equilibrium.

B. Migration of an oblate particle

In previous studies on inertial migration in channels, the assumption was predominantly that particles were rigid and spherical. However, in real suspensions, particles often exhibit nonspherical shapes. The rotation and migration of nonspherical particles in microfluidics are more complex than that of spherical particles. For example, nonspherical particles may display various modes such as kayaking, log rolling, and tumbling[30]. In this section, the inertial migration of oblate particles (Ar $= 0.5$) in a triangular channel is investigated.

1. Oblate particles in triangular channels

For cases of oblate particles in triangular channels, not only the initial position but also the initial orientation may affect their equilibrium positions. Overall, eventually, there exist two rotational motion modes. Figures 14(a) and 14(b) show the log-rolling and tumbling modes, respectively. In our simulation, when particles are initially positioned along the angle bisector with a specific orientation, meaning the particle's evolution axis is inside the plane bisecting the angle, they migrate along the angle bisector to the CEP and rotate in the tumbling mode. On the other hand, for most other initial orientations and positions (excluding the angle bisector), particles reach the FEP with the log-rolling mode.

In fact, only the initial orientation condition that ultimately leads to the CEP is more sensitive (it only allows the initial appearance of tumbling, which means its symmetric axis should be inside the $y - z$ plane). For other cases that ultimately lead to the FEP, particles are independent of the initial orientation, as shown in Fig. 14(c). The orientation of the particles is described by the unit vector $n = [nx, ny, nz]$ parallel to the particle's symmetry axis. Here, to obtain more generalized conclusions, an initial orientation of $(\phi_0, \theta_0, \psi_0) = (80^\circ, 0^\circ, 0^\circ)$ is adopted.

In Fig. 15(a), we present the migration trajectories of particles from different initial positions. Four representative positions are selected due to the symmetry of the triangular cross section. Unlike spherical particles, oblate particles tend to migrate toward the FEP and exhibit log-rolling motion. Interestingly, we observe a similar equilibrium manifold as shown in Fig. 5, but it appears more rounded compared to the manifold of spherical particles. This curvature is correlated with the tumbling motion during the migration of oblate particles.

Figure 15(b) illustrates the time evolution of the x component of the oblate symmetry vector, n_x, for different trajectories. Taking the blue and red curves as examples, n_x initially exhibits an oscillatory upward trend, indicating a tumbling motion. After a short time ($t < 200$), it stabilizes and the particle gradually approaches the FEP in log-rolling mode.

Finally, we compare the focusing length for spherical and oblate particles in Fig. 15(c). Although the trajectories of these two particles look similar, oblate particles require a longer focusing length than spherical particles. This difference may be attributed to the rotary motion of oblate particles during migration, which may effectively reduce the lateral forces acting on them, resulting in a longer focusing length.

2. Effect of particle size

In this section, we focus on the influence of particle size on inertial migration while maintaining Re $= 20$ and Ar $= 0.5$. Our investigation encompasses three distinct sizes denoted as small, medium, and large particles, corresponding to $\beta = 0.23, 0.35, 0.46$, respectively. Notably, Figs. 16(a)–16(c) present representative migration trajectories and motion modes for each particle size category. It is evident that the

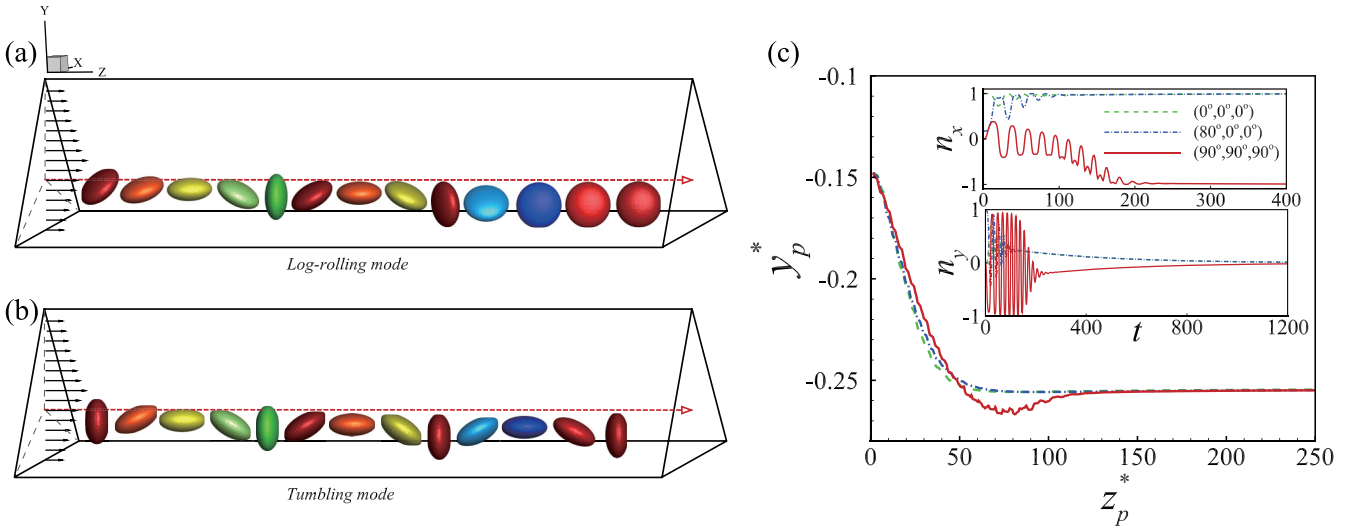

FIG. 14. Evolution of an oblate particle from its initial state to equilibrium states: (a) Log-rolling mode. (b) Tumbling mode. (c) Variation of equilibrium positions and x, y components of the orientation vector (n_x, n_y) $(n_z = 0)$ with particle migration for different initial orientations.

small particle migrates toward the FEP, characterized by log-rolling rotation. Conversely, the medium and large particles follow a trajectory that initially brings them closer to the wall, followed by migration parallel to the wall towards the CEP. This motion is also coupled with log-rolling rotation.

Figures 16(d) and 16(e) present the variations of focusing length and n_x over time for the cases with different β. Interestingly, the medium particles seem to exhibit a special state. In Fig. 16(d), before $z_p^* < 600$, the migration process of the small and medium particles is same. At this point, the medium particles are in a transient equilibrium state. However, when $z_p^* > 600$ and $t < 1000$, the medium particles start to rotate with an inclination to the original rotation axis, but still in log-rolling mode, moving along the trajectories parallel to the wall towards CEP. Eventually, the major axis of the particles coincides with the angle bisector, corresponding to $n_x = 0.5$. But for the large particles, there is no pause process like medium particles before $t < 1000$.

3. *Effect of Reynolds number*

In this section, we focus on the influence of Re on the migration dynamics of oblate particles. We consider a range of

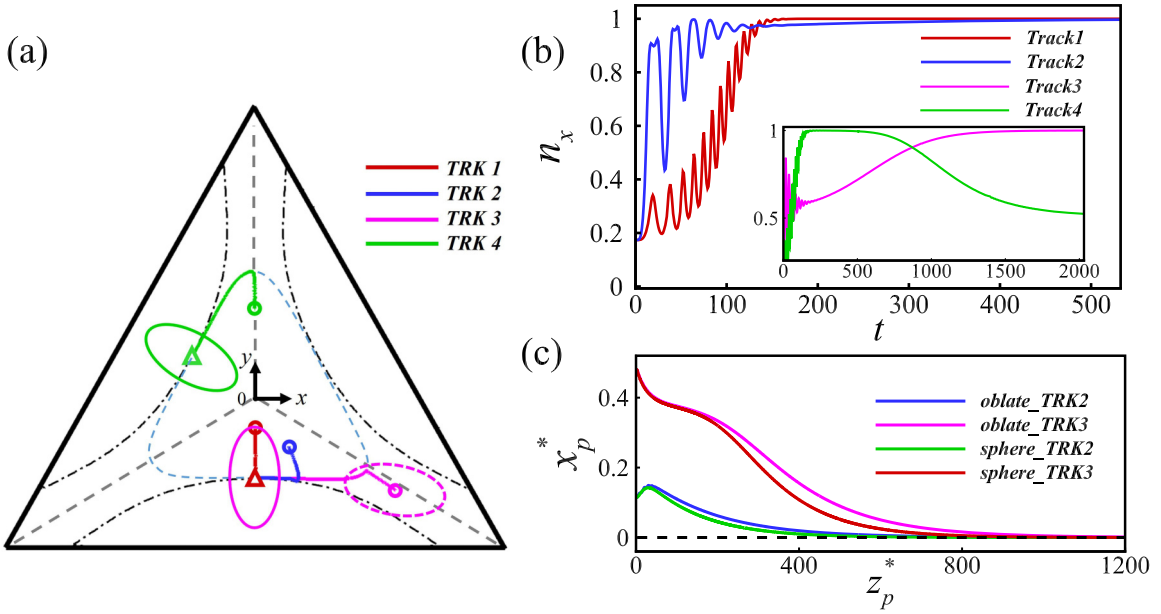

FIG. 15. (a) Inertial migration of oblate particles in an equilateral triangular channel from different initial positions. The dashed ellipses represent the initial states of the particles, while the solid ellipses represent typical snapshots at the final states. Re = 20, $\beta = 0.23$, $(\phi_0, \theta_0, \psi_0) = (80°, 0°, 0°)$. (b) The x component of the orientation vector, n_x, as a function of time for the different initial positions. (c) The nondimensional position x_p^* of the particle during the migration process as a function of the nondimensional focusing length. The black dashed line represents the x_p^* at the equilibrium position.

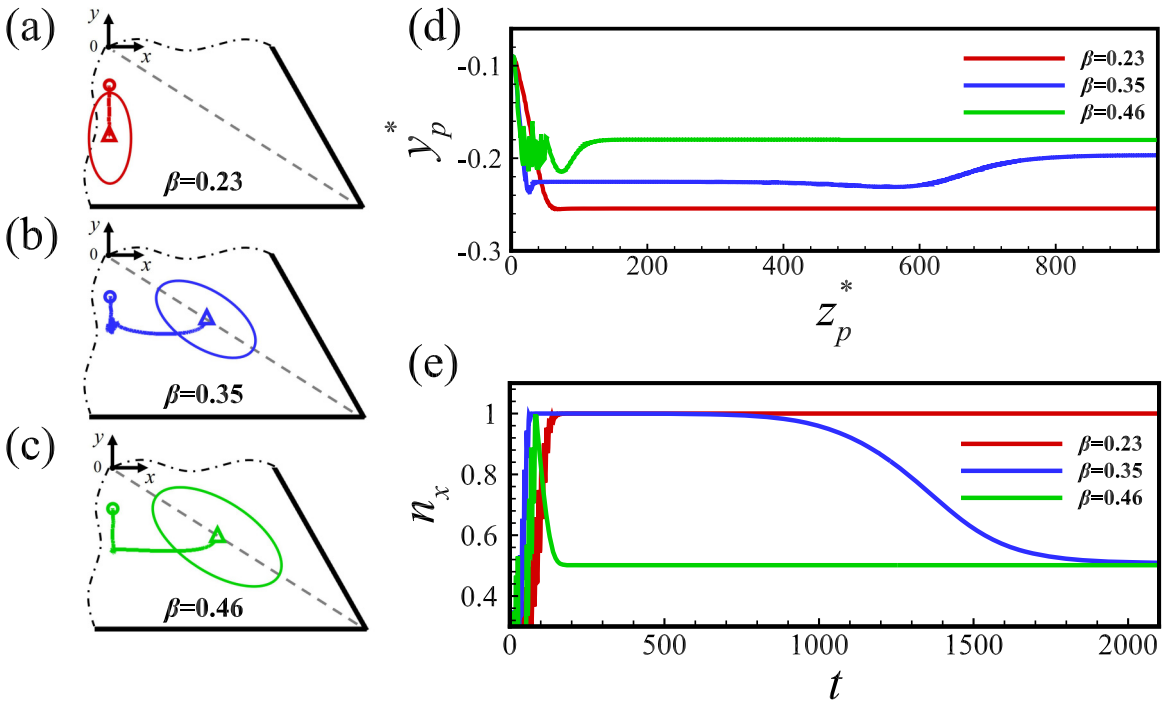

FIG. 16. (a)–(c) The lateral migration trajectories (thick solid lines) of oblate particles with different sizes. The solid ellipses represent the final states of the particles. In all cases, Re = 20. (d) The nondimensional position y_p^* of the particle during the migration process as a function of the nondimensional focusing length. (e) The x component of the orientation vector, n_x, as a function of time for the different β. In all figures, pink, yellow, and blue represent the cases of $\beta = 0.23$, 0.35, and 0.46, respectively.

Re values from 20 to 200 with an increment of 20. Throughout our analysis, β is held at 0.23, and Ar is maintained at 0.5. The initial position of each case is $(x_p^*, y_p^*) = (0.23, -0.2)$, which is a typical general initial location. Remarkably, our observations reveal that oblate particles exhibit migration towards the FEP across all Re values. Additionally, irrespective of the circumstances, oblate particles consistently engage in log-rolling motion, aligning their long axis parallel to the x axis.

Figure 17(a) graphically depicts the dimensionless equilibrium positions of both spherical and oblate particles in relation to Re. Notably, for oblate particles, their equilibrium positions decrease when Re < 120, indicating closer proximity to the channel wall. This trend shifts as Re surpasses 120, leading to a gradual increase in equilibrium positions, albeit with less pronounced significance. A similar curve for spherical particles is superimposed on the graph, demonstrating an analogous growth pattern. Both curves exhibit a pivotal inflection point at approximately Re ≈ 120. This phenomenon has been previously addressed in our discussion on the distribution of the lift coefficient on particles within the pipeline (Sec. III A 3). However, owing to the log-rolling motion inherent to oblate particles at equilibrium, the upward shift of the FEP is marginally slower when compared to spherical particles.

Turning our attention to Fig. 17(b), we present the temporal evolution of the x-component symmetry vector, n_x, for particles at Re = [40, 120, 200]. At varying Re levels, oblate particles undergo a brief period of tumbling motion during their migration, occurring within the time interval t = 0–130. Subsequently, they gradually transition into log-rolling mode. It is worth noting that the frequency of tumbling motion diminishes at higher Re, evident in the smoother fluctuations depicted in the curves. Importantly, the time required for particles to achieve stability lengthens with increasing Re, indicating an extended duration for n_x to approach unity (1).

4. The transition between the FEP and CEP of oblate particles

However, the transition Reynolds number increases from 120 to 140 for oblate particles. We deduce that this delay in the transition is due to the tumbling motion of the particles during migration, which weakens the effect of fluid on particles.

The investigation addressed in this section is aligned with Sec. III A 4. When particles are in general initial positions, the ultimate equilibrium can be influenced by β and Re. This transition phenomenon will be explored within the context of oblate particles in triangular channels, with Ar = 0.5 being considered.

Figure 18 illustrates the phase diagrams within the (Re, β) parameter space. It is evident that larger particles ($\beta >$ 0.4) tend to migrate toward the CEP. This can be geometrically reasoned as these particles undergo log-rolling motion at the FEP. Eventually, the particle's long axis becomes perpendicular to the wall, rendering the FEP less accommodating for larger particles. For particles of medium size ($0.15 < \beta < 0.4$), the sole equilibrium position remains at the FEP.

For smaller particles ($\beta = 0.12$), an equilibrium position shift from FEP to CEP occurs around Re ≈ 140. We have pre-

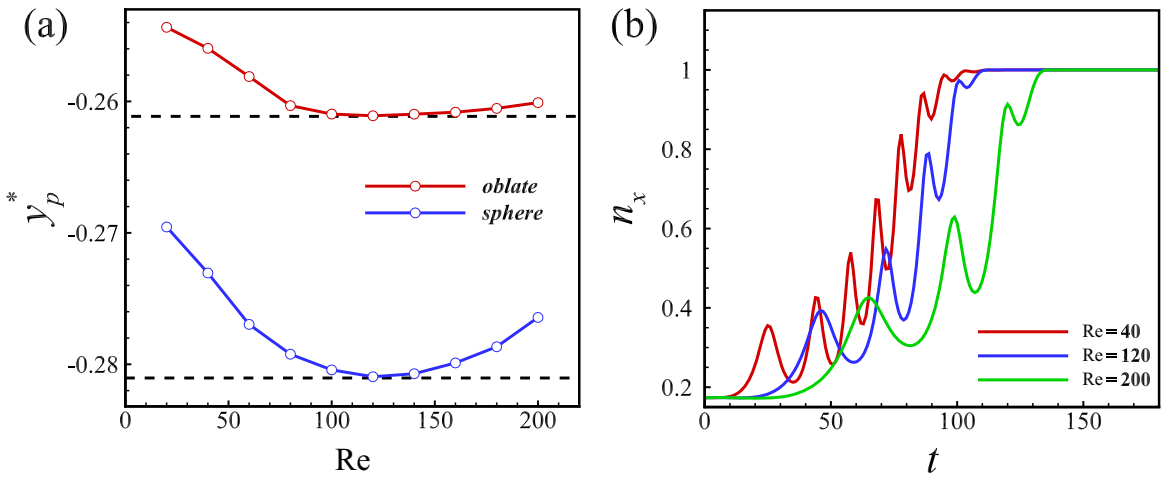

FIG. 17. (a) The nondimensional equilibrium position y_p^* of the particle as a function of Re. The red curve represents the oblate particles. The blue represents the sphere. (b) The x component of the orientation vector, n_x, as a function of time for Re = [40, 120, 200].

viously examined this phenomenon in the context of spherical particles, offering a coherent explanation based on inertia and stability considerations.

IV. CONCLUSION

In this investigation, we employ the IMB-LBM method to explore the inertial migration of both spherical and oblate particles within an equilateral triangular channel. For spherical particles, two distinct equilibrium positions emerge: the corner equilibrium position is situated along the angle bisector near the corner, while the face equilibrium position is located on a segment of the line perpendicular from the triangle's center to one of its sides. In the majority of cases under investigation, particles that are initially situated along the bisector ultimately converge towards the CEP, whereas those with initial positions not aligned along the angle bisector typically demonstrate migration towards the FEP.

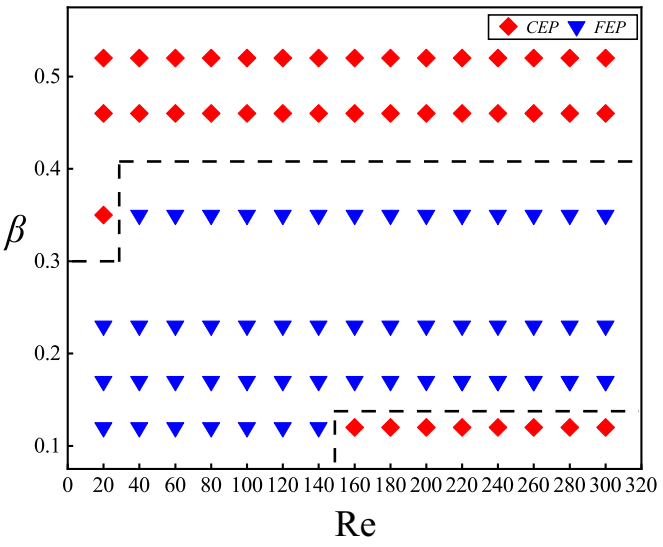

FIG. 18. Phase diagram of particle equilibrium positions in (Re, β) parameter plane, Ar = 0.5. The initial position of each point is $(x_p^*, y_p^*) = (0.23, -0.2)$, which is a typical general initial location.

Shifting our focus to oblate particles, similar to spherical counterparts, they display two equilibrium positions. However, their behavior is characterized by distinct rotational modes: log rolling and tumbling. The stability of the CEP depends on the particle's initial position and orientation. To achieve equilibrium at the CEP, the particle must commence its motion positioned along the angle bisector, with an orientation facilitating tumbling around an axis parallel to the x axis. Alternatively, particles will migrate toward the FEP and undergo log-rolling rotation.

Examining the ultimate equilibrium configurations of particles with general initial positions, we construct a comprehensive phase diagram within the parameter space defined by Re and β. Significantly, the insights derived from our study are universally applicable to both spherical and oblate particles. In the case of larger particles, a tendency is observed wherein they migrate towards the CEP. This phenomenon can be rapidly comprehended through geometric reasoning: given the proximity of the FEP to the wall, it becomes impractical for larger particles to occupy this position. Consequently, their migration is inevitably directed towards the CEP.

Smaller particles undergo an inertia-driven transition from the FEP to the CEP equilibrium state. As Re rises, fluid inertia becomes more influential. The movement of these smaller particles is predominantly governed by the fluid flow. Consequently, the fluid guides these particles towards the CEP, characterized by reduced flow velocity and a gentler shear gradient.

In the cases of a specific particle with different Re, we observed an initial retreat of the FEP position from the channel center as Re increases, followed by a subsequent return towards the center. This phenomenon can be elucidated through forces. As Re increases, the region where the shear-induced lift force and rotation-induced lift force dominate moves up.

Consequently, particles are drawn nearer to the wall. However, with a further elevation of Re, the proximity between particles and the wall diminishes, leading to a pronounced surge in the wall-induced lift force, thereby propelling particles away from the wall. Our findings have the potential to illuminate particle manipulation within microchannels and offer insights that could contribute to the design of a wide range of applications.

ACKNOWLEDGMENT

This work is supported by the Natural Science Foundation of China (NSFC), Grant No. 11772326. This project is also supported by the Joint Funds of the National Natural Science Foundation of China (Grant No. U21B2070). In addition, this research is supported by the Supercomputing Center of the USTC.

[1] J. M. Martel and M. Toner, Inertial focusing in microfluidics, Annu. Rev. Biomed. Eng. **16**, 371 (2014).

[2] T. Tohme, P. Magaud, and L. Baldas, Transport of non-spherical particles in square microchannel flows: A review, Micromachines **12**, 277 (2021).

[3] J.-A. Kim, J. Lee, C. Wu, S. Nam, D. Di Carlo, and W. Lee, Inertial focusing in nonrectangular cross-section microchannels and manipulation of accessible focusing positions, Lab Chip **16**, 992 (2016).

[4] G. Segre and A. Silberberg, Radial particle displacements in Poiseuille flow of suspensions, Nature (London) **189**, 209 (1961).

[5] P. G. Saffman, The lift on a small sphere in a slow shear flow, J. Fluid Mech. **22**, 385 (1965).

[6] R. Repetti and E. Leonard, Segré-Silberberg annulus formation: A possible explanation, Nature (London) **203**, 1346 (1964).

[7] B. Ho and L. Leal, Inertial migration of rigid spheres in two-dimensional unidirectional flows, J. Fluid Mech. **65**, 365 (1974).

[8] P. Vasseur and R. Cox, The lateral migration of a spherical particle in two-dimensional shear flows, J. Fluid Mech. **78**, 385 (1976).

[9] D. Farajpour, A review on the mechanics of inertial microfluidics, J. Comput. Appl. Mech. **52**, 168 (2021).

[10] J. Matas, J. Morris, and E. Guazzelli, Lateral forces on a sphere, Oil Gas Sci. Technol. **59**, 59 (2004).

[11] E. S. Asmolov, The inertial lift on a spherical particle in a plane Poiseuille flow at large channel Reynolds number, J. Fluid Mech. **381**, 63 (1999).

[12] J.-P. Matas, J. F. Morris, and E. Guazzelli, Lateral force on a rigid sphere in large-inertia laminar pipe flow, J. Fluid Mech. **621**, 59 (2009).

[13] J.-P. Matas, J. F. Morris, and É. Guazzelli, Inertial migration of rigid spherical particles in Poiseuille flow, J. Fluid Mech. **515**, 171 (2004).

[14] S. Nakayama, H. Yamashita, T. Yabu, T. Itano, and M. Sugihara-Seki, Three regimes of inertial focusing for spherical particles suspended in circular tube flows, J. Fluid Mech. **871**, 952 (2019).

[15] D. Di Carlo, D. Irimia, R. G. Tompkins, and M. Toner, Continuous inertial focusing, ordering, and separation of particles in microchannels, Proc. Natl. Acad. Sci. **104**, 18892 (2007).

[16] I. Lashgari, M. N. Ardekani, I. Banerjee, A. Russom, and L. Brandt, Inertial migration of spherical and oblate particles in straight ducts, J. Fluid Mech. **819**, 540 (2017).

[17] B. Chun and A. Ladd, Inertial migration of neutrally buoyant particles in a square duct: An investigation of multiple equilibrium positions, Phys. Fluids **18**, 031704 (2006).

[18] N. Nakagawa, T. Yabu, R. Otomo, A. Kase, M. Makino, T. Itano, and M. Sugihara-Seki, Inertial migration of a spherical particle in laminar square channel flows from low to high Reynolds numbers, J. Fluid Mech. **779**, 776 (2015).

[19] P. Mukherjee, X. Wang, J. Zhou, and I. Papautsky, Single stream inertial focusing in low aspect-ratio triangular microchannels, Lab Chip **19**, 147 (2019).

[20] J.-A. Kim, A. Kommajosula, Y.-H. Choi, J.-R. Lee, E.-C. Jeon, B. Ganapathysubramanian, and W. Lee, Inertial focusing in triangular microchannels with various apex angles, Biomicrofluidics **14**, 024105 (2020).

[21] D. Noble and J. Torczynski, A lattice-Boltzmann method for partially saturated computational cells, Intl. J. Mod. Phys. C **09**, 1189 (1998).

[22] Z. Guo, C. Zheng, and B. Shi, Discrete lattice effects on the forcing term in the lattice Boltzmann method, Phys. Rev. E **65**, 046308 (2002).

[23] B. K. Cook, D. R. Noble, and J. R. Williams, A direct simulation method for particle-fluid systems, Eng. Comput. **21**, 151 (2004).

[24] Y. Feng, K. Han, and D. Owen, Combined three-dimensional lattice Boltzmann method and discrete element method for modelling fluid-particle interactions with experimental assessment, Intl. J. Numer. Methods Eng. **81**, 229 (2010).

[25] C. R. Leonardi, J. W. McCullough, B. D. Jones, and J. R. Williams, Electromagnetic excitation of particle suspensions in hydraulic fractures using a coupled lattice Boltzmann-discrete element model, Comput. Part. Mech. **3**, 125 (2016).

[26] B. H. Yang, J. Wang, D. D. Joseph, H. H. Hu, T.-W. Pan, and R. Glowinski, Migration of a sphere in tube flow, J. Fluid Mech. **540**, 109 (2005).

[27] M. Bouzidi, M. Firdaouss, and P. Lallemand, Momentum transfer of a Boltzmann-lattice fluid with boundaries, Phys. Fluids **13**, 3452 (2001).

[28] J. Zhou and I. Papautsky, Fundamentals of inertial focusing in microchannels, Lab Chip **13**, 1121 (2013).

[29] P. Cherukat and J. B. McLaughlin, The inertial lift on a rigid sphere in a linear shear flow field near a flat wall, J. Fluid Mech. **263**, 1 (1994).

[30] H. Huang and X.-Y. Lu, An ellipsoidal particle in tube Poiseuille flow, J. Fluid Mech. **822**, 664 (2017).